AIAA JOURNAL
Vol. 51, No. 2, February 2013

# Heated Helium to Simulate Surface Pressure Fluctuations Created by Rocket Motor Plumes

J. Panda,* N. J. Burnside,† R. K. Fong,‡ and J. C. Ross‡
*NASA Ames Research Center, Moffett Field, California 94035*
and
G. H. James§ and V. A. Fogt§
*NASA Johnson Space Center, Houston, Texas 77058*

DOI: 10.2514/1.J051485

**The solid-rocket plumes from the abort motor of the multipurpose crew vehicle were simulated using hot, high-pressure, helium gas to determine pressure fluctuations on the vehicle surface in the event of an abort. About 80 different abort situations over a Mach number range of 0.3 to 1.2, and vehicle attitudes of $\pm 14$ deg, were simulated using a 6% scaled model inside the NASA Ames Transonic Wind Tunnel. The test showed very high level of surface pressure fluctuations caused by the hydrodynamic near-field of the plume shear layer. The plumes grew in size with increasing flight Mach number, which was associated with a lowering of the ambient pressure. This caused an increase of plume impingement on the vehicle. Interestingly, the trend was a decrease in the level of pressure fluctuations with increasing impingement. The wind-tunnel data were compared against flight data from the Pad Abort 1 flight test. Despite various differences between the transient-flight situation and the steady-state wind-tunnel simulations, the hot-helium data were found to replicate Pad Abort 1 fairly reasonably. The data gathered from this one-of-a-kind wind-tunnel test fills a gap in the manned-space programs, and will be used to establish the acoustic environment for vibro-acoustic qualification of the multipurpose crew vehicle.**



## Nomenclature

| | | |
|---|---|---|
| $Cp_{rms}$ | = | $p_{rms}/q_j$, normalized pressure fluctuations |
| $c$ | = | speed of sound |
| $D$ | = | nozzle diameter |
| $f$ | = | frequency |
| $I$ | = | turbulence intensity |
| $J$ | = | momentum flux in plume/freestream |
| $M$ | = | Mach number |
| $m$ | = | molecular weight |
| $p$ | = | pressure |
| psd | = | power spectral density |
| $q$ | = | $\frac{1}{2}\rho u^2$ ($\frac{1}{2}\gamma$pM$^2$) dynamic pressure |
| $R$ | = | universal gas constant |
| $Re$ | = | Reynolds number |
| $St$ | = | $fD/U$, Strouhal frequency |
| $t$ | = | temperature |
| $U$, $u$ | = | velocity |
| $We$ | = | mechanical power per unit nozzle area |
| $\alpha$ | = | angle of attack |
| $\beta$ | = | sideslip angle |
| $\gamma$ | = | ratio of specific heats |
| $\theta$ | = | azimuthal angle |
| $\rho$ | = | density |
| $\tau$ | = | time |

*Subscripts*

| | | |
|---|---|---|
| $a$ | = | ambient/freestream condition |
| $e$ | = | nozzle exit condition |
| $f$ | = | full-scale flight condition |
| $h$ | = | helium plume conditions |
| $j$ | = | fully expanded plume condition |
| $r$ | = | rocket-motor plume conditions |
| $t$ | = | wind-tunnel freestream condition |
| | = | plenum/total condition |
| $i$, $k$ | = | indices for repititive sum over 1, 2, 3 |

Presented as Paper 2011-2901 at the 17th AIAA/CEAS Aeroacoustics Conference, Portland OR, 5–8 June 2011; received 6 July 2011; revision received 23 February 2012; accepted for publication 27 February 2012; published online 4 January 2013. 

*Engineer, Flight Vehicle Acoustics, Experimental Aero-Physics Branch, Associate Fellow AIAA.
†Engineer, Flight Vehicle Acoustics, Experimental Aero-Physics Branch, Senior Member AIAA.
‡Engineer, Fluid Mechanics, Experimental Aero-Physics Branch.
§Engineer, Structural Mechanics, Loads and Structural Dynamics Branch.

## I. Introduction

THE launch-abort vehicle (LAV) is intended to separate the crew module from the rest of the rocket vehicle in case of an emergency. This is achieved via firing a high-thrust, solid-rocket motor, called the abort motor (AM), attached to the apex of the LAV (Fig. 1). High-velocity and high-temperature plumes from the solid rocket flows from four nozzles canted approximately 20 deg to the vehicle axis. The plume flows above the boost protective cover (BPC) that surrounds the front part of the crew module. The radiated and hydrodynamic fluctuations in the high-speed rocket plumes are expected to create intense surface pressure fluctuations over large portions of the vehicle surface. The acoustic environment from the AM is unique to this configuration of a crewed space vehicle and far exceeds all acoustic levels encountered during liftoff, ascent through the atmosphere (transonic and maximum dynamic pressure phases), and reentry phases of a nominal flight.

An important part of a spacecraft design is the vibro-acoustic certification of all components via rigorous testing in reverberant chambers and on shaker tables. The surface pressure fluctuations on the vehicle are the primary contributor to the acoustic and vibrational levels used for these qualification tests. It is expected that the limiting environment for most of the structural components, propulsive systems and electronic and navigational subsystems and life-support system of the multipurpose crew vehicle (MPCV) and the LAV will arise from the firing of the abort motor.

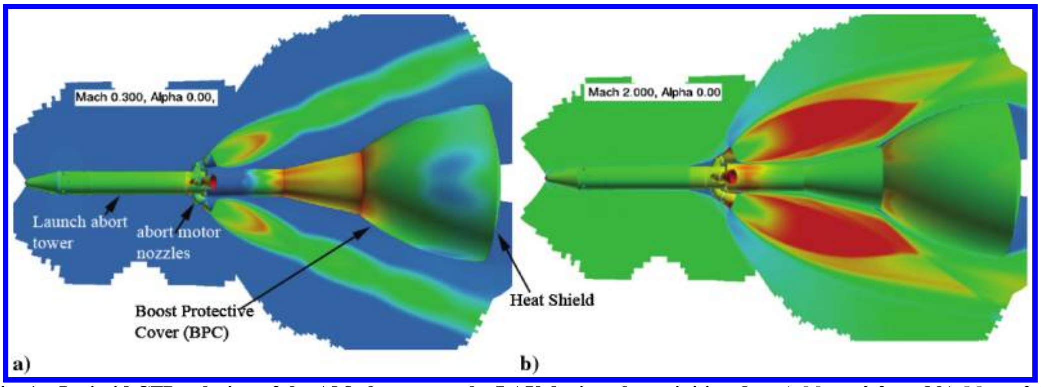


**Fig. 1 Inviscid CFD solution of the AM plume over the LAV during aborts initiated at a) $M_f = 0.3$, and b) $M_f = 2.0$.**

Unfortunately, limited guidance was available to charaterize abort acoustics from past manned space programs that used a similar launch-abort concept including Apollo, Mercury, and Gemini, and the Space Shuttle did not use a rocket-firing-based abort scenario. There are reports of the use of unsteady pressure transducers in one of the abort test flights from the Apollo era; however, actual data were unavailable and not recovered.

As a first step toward an understanding of the plume flowfield, results from computational fluid dynamics (CFD) simulations were used in the current program. Figure 1 shows the Mach number distributions in the flight stream and inside the plume at flight Mach numbers of 0.3 and 2.0, and at $\alpha = \beta = 0$ (same color scale, corresponding to the Mach number distribution, is used for both figures). Although CFD can provide estimates of the time-averaged flow properties, the current capbilities of large-eddy simulation and direct numeical simulation fall short of estimating the unsteady pressure fluctuations for the large Reynolds number and wide Strouhal frequency range necessary for the present application. Lack of a database and low confidence in the prediction schemes made it impossible to determine the acoustics fluctuations for the design of a safe vehicle. This led to a emperically based strategy consisting of several tests to establish the vibro-acoustics environemnt for the MPCV and the LAV. The present hot-helium test, designateded 80-AS, is a part of that test program. So far, the other parts of this campaign are 1) static-fire test of the AM, 2) unmanned flight test Pad Abort 1 (PA1), and 3) another wind-tunnel test, designated 51AS, where mildly heated compressed air was used to simulate the abort plumes. The use of solid rocket motors in transonic wind tunnels was studied as an alternate to the present test; however, the effort was found to be cost-prohibitive.

This report focuses on the 80-AS hot-helium test. The primary goals are 1) summarize considerations leading to the selection of helium to simulate the rocket plumes, 2) present the relationships needed to scale the model-scale helium plume data to the full scale flight vehicle, 3) present selected sample results, and 4) compare model-scale wind-tunnel data with full-scale flight data collected from the PA1 vehicle.

There is a need to clarify terms “acoustics” and “surface pressure fluctuations” that are used interchangeably in the text. The purpose of the present work is to determine pressure fluctuations on the surface of the LAV. Typically, in jet-noise literature, acoustics refers to the pressure fluctuations that have radiated out to the far field. However, in rocket-vehicle literature, acoustics is used in a broader sense, a norm followed in the present paper, to include any type of surface pressure fluctuations. Strictly speaking the pressure fluctuations on the LAV surface is caused by both radiatiave and nonradiative parts of the hydrodynamic field created by the rocket plumes.

### A. Case for Helium

Reorganization of the exact equations of motion, Navier–Stokes and continuity, shows that the pressure fluctuations $p(\boldsymbol{X}, \tau)$ at a point $\boldsymbol{X}$ on a rigid body is given by a volume integral of the turbulent fluctuations in its neighborhood. The turbulent fluctuations are expressed through Lighthill’s turbulence stress tensor $\boldsymbol{T}_{ik}$ [1]:

$$p(\boldsymbol{X}, \tau) = \frac{1}{2\pi} \int_V \frac{\partial^2 \boldsymbol{T}_{ik}}{\partial Z_i \partial Z_k} \left(\boldsymbol{Z}, \tau - \frac{r}{c}\right) \frac{\mathrm{d}\boldsymbol{Z}}{r} \tag{1}$$

Here, $\boldsymbol{Z}$ is a position vector within the volume, and $r$ is the distance separating the point source $\boldsymbol{Z}$ from the position on the surface $\boldsymbol{X}$, $r = |\boldsymbol{Z} - \boldsymbol{X}|$. Neglecting the viscous contributions, which are deemed secondary, the Lighthill stress tensor is expressed as follows:

$$\boldsymbol{T}_{ik} = \rho u_i u_k + \delta_{ik}(p - c^2 \rho) \tag{2}$$

Here, $u_i$ and $u_k$ are velocity componenets along the $i$ and $k$ directions, and $\delta$ is the Kronecker delta. Although the previous equation cannot be used directly, it provides the necessary guidance for setting up an acoustic test using a substitute gas. It shows that there are two primary variables: 1) fluctuations in $\rho u_i u_k$ (related to the local dynamic pressure), and 2) entropy fluctuations associated with changes in $(p - c^2 \rho)$. In a low-speed isentropic flow, the second term is insignificant, whereas in a solid rocket plume, it may be of importance.

At first glance, helium and the rocket plume appear to be vastly different. The chemical composition of helium (inert gas) is certainly different from that of a solid rocket plume ($Al_2O_3$ powder, steam, $H_2$, HCl, CO, $CO_2$, etc.). There are also significant differences in the molecular weight, specific heat, thermal conductivity, etc. However, Eqs. (1) and (2) show that these parameters do not directly influence the noise-generation properties of jet plumes. For noise generation, the important parameters are plume velocity, sound speed, density, and plume size. Among the different choices of the substitute gas, heated helium is found to provide the closest match to a rocket plume for the aforementioned acoustically relevant parameters. There are other derived parameters, such as Mach number and static pressure ratio at the nozzle exit, used in various noise modeling. If this list needs to be shortened to one central parameter, then it is the very high speed of sound at low tepmerature that makes helium the most suitable substitute gas. At temperature $t$, the sound speed in a gas is given by $c = \sqrt{\gamma R t / m}$. The sound speed in the ambient temperature helium is nearly three times that of air and is close to that of a solid rocket plume. The only other gas that has a faster sound speed is hydrogen, preceding helium in the periodic table. Hydrogen is extremely combustible, making it unsuitable for use in the confinements of a wind tunnel. Although the sound speed of helium at ambient temperature is similar to that of a rocket plume, the static temperature of a compressed gas decreases as it is expanded through a nozzle. To compensate for this decrease in temperature, additional heating of helium is required. Heating of pure helium brings the velocity of the resulting jet close to that of a rocket plume. Finally, gas density $\rho = pm/Rt$ is a function of the molecular weight, which is far lower for helium than rocket plume. Therefore, helium is able to replicate the low density of a solid rocket plume at a lower chamber pressure and temperature than that of a rocket motor. Note that the fluctuations of temperature and the ratio of specific heat do not enter directly in Eq. (1). Therefore, gases with dissimilar $\gamma$ can produce the same pressure fluctuations if heated to a different temperature. In summary, similarity of sound speed, plume speed, plume density, and safe handling properties of helium were the primary motivations for choosing it as the rocket-plume stimulant.

The primary differences between helium and the plume of a solid rocket motor arise due to three factors: 1) lack of afterburning, 2) lack of particle damping, and 3) mismatch in the ratio of specific heat. The presence of the unburned fuel and combustible chemicals produces afterburning in the rocket plume, which cannot be reproduced in helium. Equation (2) shows that entropy fluctuations are a source of pressure fluctuations, and the combustion process in the shear layer of a rocket plume is expected to produce some entropy fluctuations. However, estimates of its impact were not found in the existing literature.

The influence of the solid $Al_2O_3$ powder in the solid rocket plume can also not be replicated in the helium simulation. It is known that the presence of solid particles can reduce the sound speed, cause attenuation of sound waves, and help break down the shock system [2,3]. This could lead to a lowering of the radiated noise at some frequency bands. Additionally, the mismatch in the ratio of specific heats makes matching both density and sound speeds between a helium and a rocket plume difficult. Finally, the diameter of an underexpanded helium plume is smaller than that of a comparable rocket. All of these bring about a set of flow parameters, some of which can be matched between a helium and rocket plume and some cannot. In spite of these differences, the helium simulation was found to replicate flight data from the actual motor burn reasonably well. The effect of various choices made in the past experiments is discussed next.



### B. Past Experience of Using Helium to Simulate Plume Noise

In the past, helium plumes were used mostly to study far-field acoustic fluctuations. Almost all of these applications involved simulating noise from the static jets without the influence of any forward flight. The present LAV application, on the other hand, involves both static firing and a large range of forward-flight conditions. To simulate the relatively low-temperature and low-velocity air plumes produced by commercial and military jet engines, typically $u/c_a \sim 1.8$ and $T_0 \sim 1400°F$, unheated helium was mixed with unheated air [4–6]. Mixing with air reduces sound speed of pure helium, and makes the mixture velocity comparable to that of the jet engines. Even for these lower-temperature simulations, not all parameters could be matched. These simulations tried to match either the sound speed or the air density of jet engine plumes. Matching the sound speed was found to provide the best result. The overall agreement between the hot air and helium–air mixture was found to be within 1.2 dB.

Recently, Greska et al. [7] and Greska and Krothapalli [8] compared the near-field pressure fluctuations of plumes of hot helium and hot air. They have proposed use of the Oertel convective Mach number $M_{co}$ to determine the acoustic similarity: $M_{co} = (u_j + \frac{1}{2}c_j)/(c_j + c_a)$. By definition, $M_{co}$ includes all relevant velocity parameters involved in sound generation and far-field radiation. They found a fair match in overall levels between the two plumes. One noticeable difference was that the peak acoustic source in a helium jet appeared closer to the nozzle exit. The difference was attributed to a shortened length of the potential core in the helium jet.

Simulation of a solid rocket plume by heated, pure helium by Morgan and Young [9] is the most relevant experiment to the present effort. The authors compared near- and far-field radiations from a solid rocket plume with those from helium plumes created via different plenum pressure and temperature conditions. The chamber pressure and temperature of the solid rocket plume were 635 psia and 6000 R, respectively, whereas those for the helium plume were varied between 44 to 344 psi and 750 to 1560 R. It should be noted that the solid rocket plumes are typically underexpanded; however, unlike cold air jets, the broadband shock noise peaks are not discernable. The "mixing noise" dominates the spectra at all polar angles. Morgan and Young observed that the best matching in the near- and far-field acoustic levels were obtained when the velocity, Mach number, and pressure at the nozzle exit were matched between the helium and the rocket plumes. In spite of the mismatch in the density, the jet mechanical power per unit nozzle area and some other parameters, the overall sound pressure levels were found to be within 2 dB for most of the microphone positions. A comparison of the frequency spectra of helium and rocket plume showed a small difference close to the nozzle exit and a larger difference farther downstream (20 nozzle diameters) from the plume. The differences were nonuniform among the third-octave bands. The point to take away is that a different set of matching conditions can lead to higher or lower levels at different frequency bands.

**Table 1 LAM plume diameter at different altitudes**

| Altitude, ft | 0 | 20,000 | 60,000 |
|---|---|---|---|
| Atmospheric pressure, psf | 2100 | 970 | 150 |
| Fully expanded plume diameter/ nozzle-exit diameter | 1.27 | 1.76 | 3.6 |

### C. Expected Influence of Launch Abort Vehicle Forward Flight

Because a rocket-motor-assisted abort can occur anywhere from Mach 0 (pad abort) through high supersonic Mach number, the surface pressure fluctuations are expected to vary significantly. There are two new physical phenomena that come into play with forward flight: 1) progressive increase in the plume diameter with altitude, and 2) distortions of the plume due to interactions with the freestream. The degree of underexpansion, expressed by the ratio of the nozzle exit pressure and the ambient pressure $(p_e/p_a)$ increases with vehicle altitude, primarily due to the lowering of the latter. As the pressure inside the plume relaxes to ambient, the diameter grows larger than the nozzle-exit diameter. Because the centerlines of the plumes lie very close to the BPC, the increase in the diameter is expected to lead to an increasing impingement on the vehicle surface. The CFD simulation of Fig. 1[¶] clearly shows this trend. A measure of the plume growth is its "fully expanded diameter" $D_j$, which can be estimated from a formula proposed by Tam and Tanna [10]:

$$\frac{D_j}{D_e} = \left(\frac{M_e}{M_j}\right)^{0.5} \left[\frac{1 + \frac{1}{2}(\gamma - 1)M_j^2}{1 + \frac{1}{2}(\gamma - 1)M_e^2}\right]^{\frac{\gamma+1}{4(\gamma-1)}} \tag{3}$$

Table 1 shows a comparison of the plume diameter at different abort altitudes. At 60,000 ft, the plume diameter is so large that the entire front side of the BPC encounters direct impingement. This leads to the conclusion that, for the high-altitude abort scenarios, fluctuations due to the direct impingement of the plume will play a critical role in the unsteady pressure environment.

The second phenomenon, namely interactions between the freestream and the plume, is far more complex. During transonic and supersonic flight regimes, a complex shock-wave pattern appears on the LAV surface. The freestream is also expected to deflect the plumes closer to the LAV surface, and a situation similar to "jets in cross flow" appears. The situation becomes more complex at a nonzero angle of attack. To gain some understanding of the underlying flow features, a computational effort was put in place. Coirier [11] used a RANS code with Menter's SST model and Sarkar's compressibility correction. Both the freestream and the plumes were assumed to be calorically perfect gas with constant molecular weight and specific heats. The goal of the computational effort was to provide a comparison between the solid-motor plume and that of the helium plume over the full-scale and model-scale LAV, respectively. A large set of solutions were obtained, covering a range of Mach number, $\alpha$ (angle of attack), and $\beta$ (sideslip angle). Figures 2 and 3 show distributions of turbulent intensity fluctuations $I =$

[¶]Greathouse, J. S., NASA Johnson Space Center, Private Communications, 2009.

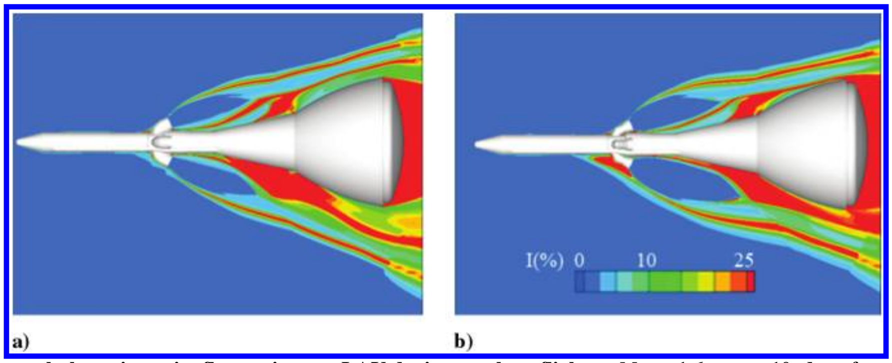


**Fig. 2 Distribution of the turbulence intensity fluctuations on LAV during an abort flight at $M_f = 1.6, \alpha = -10$ deg, $\beta = -10$ deg in a) hot-helium simulation, and b) full-scale vehicle using AM [11].**

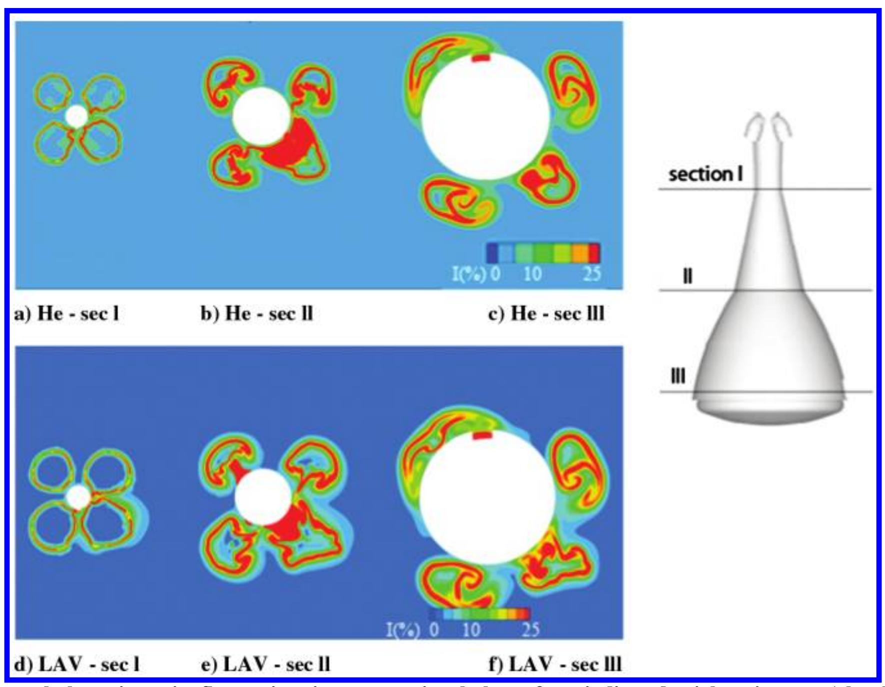


**Fig. 3 Distribution of the turbulence intensity fluctuations in cross-sectional planes from indicated axial stations: a–c) hot-helium, and d–f) full-scale LAV. All conditions are identical to Fig. 2 [11].**



$\frac{100}{U}\sqrt{\frac{2}{3}K}$ $U$ is freestream velocity, and $K$ is the turbulent kinetic energy) obtained from one such solution. Figure 2 shows the change of plume diameter in an underexpanded plume associated with the internal shock patterns. Figure 3, on the other hand, shows the appearance of "kidney vortices" and their mutual interactions, which make the three plumes cluster at the leeward side, while the remaining plume is spread over a large part of the windward side. The point to make is that the wind-tunnel simulation of the helium plume, in spite of its higher $\gamma$, makes a close duplication of the flowfield during an abort. Another observation is that the momentum ratio ($J$ is momentum in the plume/that in the freestream), a parameter characterizing the jet-in-cross-flow situations, needs to be monitored in selecting the wind-tunnel conditions.

To simulate the previously discussed forward-flight effects, the test had to be conducted in a transonic wind tunnel. The wind-tunnel conditions were not an exact match to the wide range of flight conditions expected to be encountered in the abort situations. Therefore, a scaling based on the ratio of the dynamic pressure in the flight stream $q_f$ and that in the wind-tunnel stream $q_t$ needs to be applied to the pressure-fluctuation levels measured in the wind tunnel.

Nominal ascent:

$$\frac{p'_f}{p'_t} = \left(\frac{q_f}{q_t}, \text{ other variables}\right) \tag{4a}$$

Powered abort:

$$\frac{p'_f}{p'_t} = f\left(\frac{q_f}{q_t}, \frac{q_r}{q_h}, \text{ other variables}\right) \tag{4b}$$

The scaling in Eq. (4a) is valid in the absence of a plume, such as data collected to simulate nominal flights. The presence of the plume brings a second ratio of dynamic pressures: that in the rocket plume $q_r$ to that in the helium plume $q_h$, which also needs to be accounted for.

In other words, the scaling problem, synonymously the matching problem, switches to a two $q$-ratio match.

### D. Setting Up the Test Matrix and Matching of the Plume Properties

Besides the two $q$ ratios, a host of other parameters needs to be matched for an ideal representation of the forward-flight effect. Note that the properties of underexpanded jets are expressed by two sets of parameters: those at the nozzle exit (such as $M_e$, $U_e$, $\rho_e$, pressure ratio $p_e/p_a$, etc.) and those at the fully expanded condition ($M_j$, $U_j$, $\rho_j$, $D_j$, etc.). A fully expanded condition is achieved when the pressure inside the under/over-expanded plume relaxes to the ambient condition. The CFD simulations presented previously show that the plume goes through a series of expansion–shock processes over the vehicle. The literature on underexpanded jets characterizes these changes via the use of the fully expanded conditions, which corresponds to an ideally expanded state when the plume static pressure relaxes to that of the ambient condition:

$$q_j = \frac{1}{2}\gamma p_a M_j^2, \qquad M_j = \left[\left\{\left(\frac{p_0}{p_a}\right)^{\frac{\gamma-1}{\gamma}} - 1\right\}\frac{2}{\gamma - 1}\right]^{0.5} \tag{5}$$

When the parameters associated with the fully expanded states are included, Eq. (4b) can be further expanded as

$$\frac{p_f}{p_t'} = f\left(\frac{D_{er}}{D_{eh}}, \frac{D_{jr}}{D_{jh}}, \frac{\alpha_r}{\alpha_h}, \frac{\beta_r}{\beta_h}, \frac{M_{jr}}{M_{jh}}, \frac{M_{er}}{M_{eh}}, \frac{(p_e/p_a)_r}{(p_e/p_a)_h}, \frac{c_{jr}}{c_{jh}}, \frac{\rho_{jr}}{\rho_{jh}}, \frac{\rho_{er}}{\rho_{eh}}, \frac{U_{jr}}{U_{jh}}, \frac{U_{er}}{U_{eh}}, \frac{(J_e/J_a)_r}{(J_e/J_a)_h}, \frac{W_{er}}{W_{eh}}, \frac{q_f}{q_t}, \frac{q_{jr}}{q_{jh}}\right) \tag{6}$$

The parameter space is large because many of the same variables have to be considered for both at the nozzle exit and at fully expanded conditions. Figure 4 shows the extent of the match in some critical parameters between the abort flights and the wind-tunnel simulation. To maximize the number of variables that could be closely matched within the limits of the available helium supply, typically two different combinations of helium and wind-tunnel conditions were used to simulate one abort scenario. These were called the "nozzle-exit match" and the "$q$-ratio match" conditions.

*1. Nozzle-Exit Match*

Following the guidelines from prior works (Sec. I.A), various flow parameters from the nozzle exit plane of the rocket plume were matched in this set of run conditions. Although a reasonable match in the nozzle-exit conditions was achieved using helium, still there were some differences. In Sec. I.F, a scaling law to account for these deficiencies is described. Another point to note is that, to match the nozzle-exit Mach number $M_e$ of the flight vehicle, the throat diameter of the helium model had to be larger than what simple geometric scaling dictates. These nozzle-exit match points required operating the helium plume at the highest available temperature and pressure conditions.

*2. q Ratio Match*

To satisfy the need to match two $q$ ratios of Eq. (4b), a set of operating parameters were chosen such that the ratio of the dynamic pressures between the plume $q$ and the flight $q$ is maintained in the wind-tunnel simulation:

$$\frac{q_{jr}}{q_f} = \frac{q_{jh}}{q_t} = q\text{ratio} \tag{7}$$

The motivation was that, when a scaling law based on the plume properties was applied to the wind-tunnel data, the $q$-ratio matched condition would automatically account for the differences in the freestream dynamic pressures. Compared to the nozzle-exit match, the $q$-ratio match required operating the wind-tunnel freestream at higher dynamic pressure (i.e., Reynolds number) while lowering the helium chamber pressure. On the upside, these data points required less helium; however, the aerodynamic load on the sting holding the model became very high. Some of the high-Reynolds-number conditions at the highest Mach number settings of $M = 1.05$ and 1.2 could not be achieved due to excessive sting deflections. In such situations, the tunnel Reynolds numbers were brought down to the acceptable sting deflections.

In addition to the two aforementioned conditions, additional low-Reynolds-number data points were taken for some Mach numbers to simulate higher altitude aborts. These points were taken with the highest possible helium pressure and the lowest possible tunnel static pressure to maximize the plume expansion. The intention was to estimate the fluctuation level for aborts happening at Mach numbers beyond the range available in the present simulations. Only a limited number of such data points were obtained in this test.

The test was conducted at the NASA Ames Unitary Plan, 11-Foot Transonic Wind Tunnel, where a host of abort conditions in the Mach number range $0.3 \leq M_t \leq 1.2$ were simulated. The original test included a wider range of forward flights, up to $M = 2.5$, but excessive costs caused a reduction in the scope of this test. Nevertheless, aborts occurring below the high transonic Mach number range are expected to provide the maximum pressure fluctuations over most of the vehicle. It was desirable to collect data at zero forward velocity (pad-abort condition); however, the possibility of permanent damage from the hot-gas accumulation limited the lowest tunnel Mach to 0.3. At the upper end, the highest Mach number achievable in the empty tunnel was 1.45; however, during this test, it was found that the large blockage caused by the gas lines that supply helium to the model limited the maximum achievable Mach number to 1.2.

The angle of attack $\alpha$ and the side-slip angle $\beta$ were varied within $\pm 14$ deg. The test was conducted at 11 different model attitudes. Basically, one quadrant of the $\alpha$-$\beta$ plane was completely covered, and a few other attitude points at the other quadrants were obtained to check for the symmetry of pressure fluctuations. Changing the model attitude was not a straightforward process. The challenge was to pass a very large quantity of hot, high-pressure helium into the model; gas temperature exceeded the maximum allowable temperature for the existing hollow strut of the 11 ft tunnel, and the velocity of the gas exceeded the limit for flexible hoses. A pair of insulated pipes was custom-built for each of the 11 model attitudes. Each pair supplied helium from the bottom of the test section to the model sting and had to be swapped to change the model attitude.

Developing the test matrix for the helium plume condition followed a complex balance between what is desirable for an ideal match, the maximum size of the helium system possible to construct within the engineering and financial limit, and the upper limit of the wind-tunnel operations. A 6% scale model was chosen so that many components from a previous test could be recycled. The maximum plenum temperature of 700°F was limited by the carbon steel pipes used for delivery of hot helium from the heater to the model and by the thermal stress limitations, where the hot helium pipe penetrated the pressure shell of the wind tunnel. The system was built to provide a maximum helium mass flux of $5.2\ \mathrm{lb} \cdot \mathrm{m/s}$ so that the total mass of helium used remained within available resources.

Figure 4 shows a comparison of various parameters achievable within the operational limitations of the 80AS test. All values are calculated using isentropic relations. The Mach number values in abscissa represent the flight Mach number for abort initiation. A higher Mach number is accompanied by a higher altitude and lower ambient pressure. As the ambient pressure falls, the extent of flow expansion inside the plume increases, which in turn drastically increases the fully expanded velocity and fully expanded diameter while reducing the fully expanded density and the dynamic pressure inside the plume. An examination of Fig. 4a shows that the nozzle exit velocity of the Helium plume was 94% of that of the actual AM; however, when the fully expanded velocity is considered, helium simulation produced still lower values that were also Mach-dependent. Similar examination can be made to all other parts of Fig. 4. Note that, like the nozzle-exit match, the $q$-ratio match also provided reasonably good correspondence of Mach number and plume velocity at the nozzle exit for all flight Mach numbers. Use of the two matching conditions improved correspondence in the fully expanded conditions; however, differences were seen in parameters such as the fully expanded velocity, nozzle-exit pressure ratio, momentum ratio, and the fully expanded diameter. Once again, the primary causes of these differences were the widely different $\gamma$ in He versus rocket plume, and the limit on the maximum plume

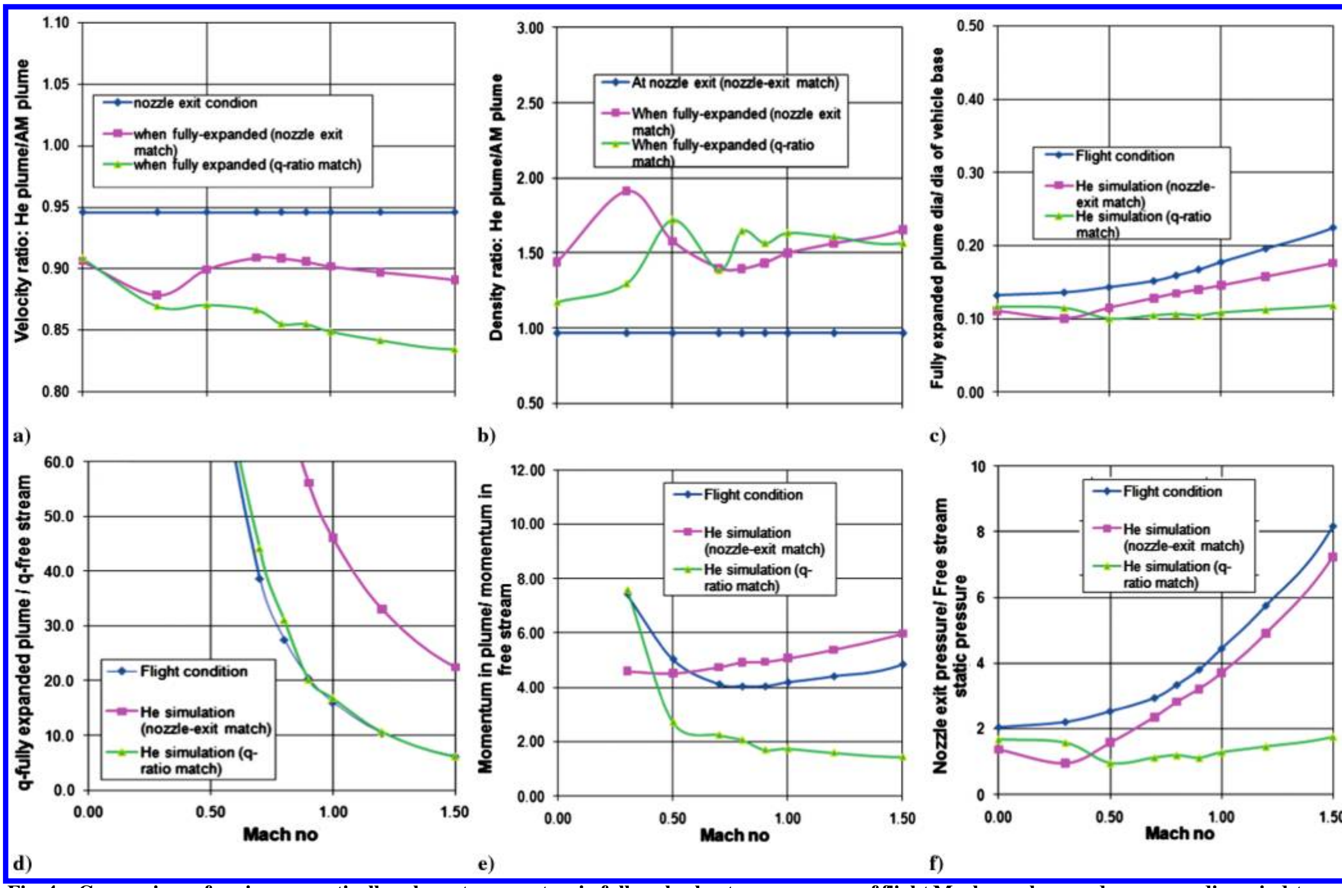


**Fig. 4 Comparison of various acoustically relevant parameters in full-scale aborts over a range of flight Mach numbers and corresponding wind-tunnel nozzle-exit match and $q$-ratio match simulations: a) plume velocity ratios $U_{eh}/U_{er}$ and $U_{jh}/U_{jr}$, b) plume density ratios $\rho_{eh}/\rho_{er}$ and $\rho_{jh}/\rho_{jr}$, c) fully expanded plume diameter as a fraction of the LAV vehicle diameter, d) $q$ ratios $q_{jr}/q_f$ and $q_{jh}/q_t$, e) momentum ratios $(J_e/J_a)_t$, and f) nozzle-exit pressure ratios $(p_e/p_a)_r$, and $(p_e/p_a)_h$.**

temperature usable in the wind tunnel. Nevertheless, it is expected that the use of scaling laws will account for many of these differences.

### E. Multipurpose Crew Vehicle Test Flight: Pad Abort 1

The Pad Abort 1 flight test took place on 6 May 2010 at the White Sands Missile Range in New Mexico (Fig. 5). A full-scale, unmanned model of the LAV was tested to verify the different phases of the flight and recovery processes for an abort scenario initiated from a launch pad [12]. In the very first phase of the flight, the AM was lit, which caused the vehicle to gain speed and altitude very quickly. The primary motor burn lasted only a couple of seconds. The outer surface of the vehicle was instrumented with 63 dynamic pressure transducers (Kulite model LL-11A-250-15A) to measure the surface pressure fluctuations. Transducer data from the first couple of seconds of the flight were analyzed and compared with the hot-helium data obtained from the present test. The flight data obviously contained changing conditions as the vehicle passed over a range of forward Mach numbers. Moreover, the PA1 vehicle was built based on an earlier design that used a slimmer outer mold line (Fig. 5a), and so the plumes were farther away from the body surface.

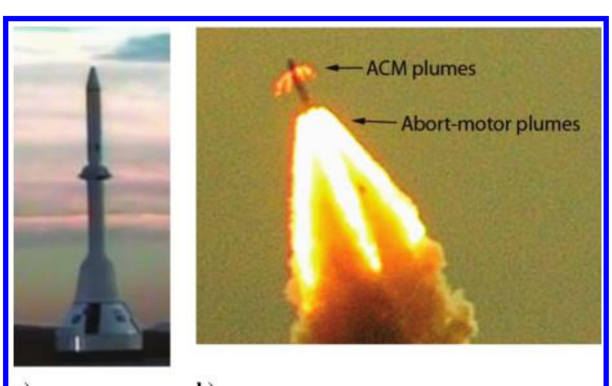


**Fig. 5 Photograph of the Pad Abort 1 vehicle a) before flight, and b) on-flight.**

**Fig. 6 Photograph of the model inside the 11 ft test section. The view is from upstream; the orange pipes brought hot helium from underneath the tunnel to the model sting.**

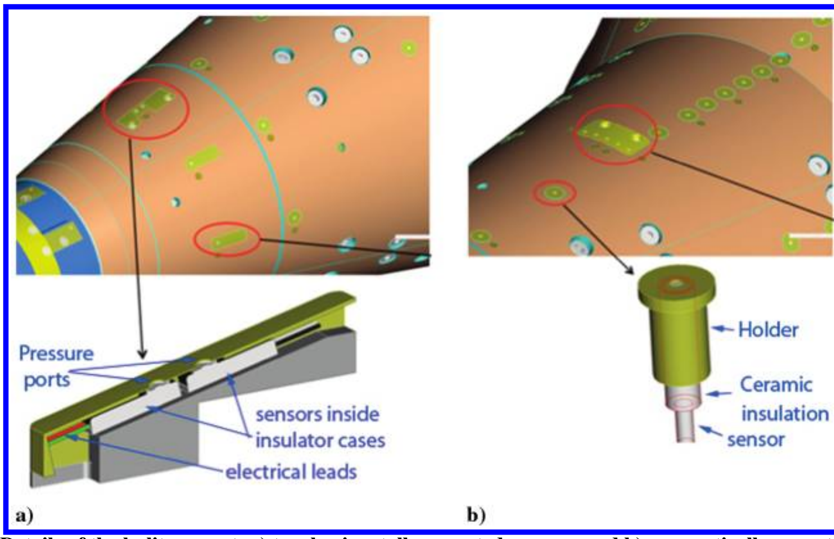


Fig. 7 Details of the kulite mount: a) two horizontally mounted sensors, and b) one vertically mounted sensor.



In spite of these differences, availability of the flight data provides a good opportunity to determine the strength and deficiencies of the helium simulations.

### F. Scale Wind-Tunnel Data to Flight Conditions

In addition to testing a small- scale model, various flow parameters between the rocket plume and the flight stream cannot be perfectly matched in a wind-tunnel test. Therefore, scaling laws need to be applied to the measured data. Observations made during the test showed that the pressure fluctuations are primarily plume-dominated. The near-field pressure fluctuations present in the plume shear layer are the primary contributor to the surface pressure fluctuations. These fluctuations are expected to scale by the dynamic pressure in the plume rather than any radiated acoustics fluctuations. Therefore, the standard dynamic pressure and Strouhal-frequency-based scaling rule should be applicable. The frequency is scaled using Strouhal number correspondence between the test and flight conditions:

$$St_{jr} = St_{jh}, \qquad f_r = f_h \frac{D_{jh}}{D_{jr}} \frac{U_{jr}}{U_{jh}} \tag{8}$$

The power spectral density (psd) levels are scaled assuming the same nondimensional overall fluctuation levels $Cp_{\mathrm{rms}}$ between the model and prototype. This leads to the following widely used relationship:

$$(\mathrm{psd}_f)_i = \left(\frac{q_{jr}}{q_{jh}}\right)^2 \frac{D_{jr}}{D_{jh}} \frac{U_{jh}}{U_{jr}} (\mathrm{psd}_t)_i$$
$$i = 1, 2, \ldots \text{number of frquency bins} \tag{9}$$

Note that the dynamic pressure $q$ and plume diameter $D$ in the previous relation corresponds to the fully expanded vales: $q_j$ & $D_j$ for the helium and rocket plumes.

Recall that the presence of the flight stream and the plume stream brings two different dynamic pressures ($q$ of the freestream, and $q$ of the plume) to the present problem. For the $q$-ratio match test points, scaling by the plume $q$, as shown in the previous equation, automatically accounts for any difference in the freestream $q$ between the wind-tunnel and flight conditions. For the rest of the test conditions, the ratio of the plume $q$ is still used for scaling. The justification is that the flowfields under and between plumes is primarily dominated by the plume rather than by the flight stream.

## II. Test Apparatus

After studying the suitability of different large wind-tunnel facilities, the Unitary Plan 11-Ft Tunnel was selected primarily because of the wide Reynolds number range available for each Mach-number condition. The wind tunnel is a closed-circuit, single-return, variable-density, continuous-flow facility that has an $11 \times 11$ ft test section. The technical details of the tunnel can be found on its website** and in [13]. The tunnel was operated in the Mach number range of 0.3 to 1.2 and in the Reynolds number range of 2e6/ft to 5e6/ft. The glass walls of the test section allowed for good shadowgraph visualization in spite of the presence of the axial slots for wall suction (to minimize shock reflection). Additionally, an infrared camera, mounted on the ceiling, was used to visualize the top part of the model. The primary goal of the IR imaging was to determine the extent of plume impingement on the model surface, thereby associating impingement with changes in pressure fluctuations over the model.

Two oxygen sensors were mounted close to the test section to monitor the helium concentration inside the tunnel. As a set of test points were collected, helium accumulated in the closed-circuit wind tunnel. To minimize this accumulation, the tunnel was periodically purged after a set of data points (typically 5 to 12) was collected. The maximum volume fraction of helium reached 15% for some test points; however, the resulting impact on $\gamma$ and the tunnel Mach number was found to be very small. The biggest impact of helium on the tunnel operation was a reduction of the freestream Reynolds number by a maximum of 10% from the set condition. This level of variation was deemed acceptable for the present data analysis.

### A. Launch Abort Vehicle Model and the Dynamic Pressure Sensors

The 6%-scale model accurately represented all details larger than 1/2 in. on the full-scale vehicle. It included four symmetric AM nozzles. The model was held by hollow sting attached to the main strut of the test section (Fig. 6). The hot helium gas was brought through the floor of the test section to the sting via two 2-in.-diam pipes. The gas then flowed upstream through the inside of the sting to a local plenum at the lower tower. Forward of the local plenum was the nozzle section, where the gas made a 160 deg turn to exit through the four nozzles. The model had stainless-steel skins and active interior cooling to ensure the survival of various instrumentations. Various other details of the model can be found in [14].

The model was heavily instrumented with 237 high-temperature, 50 psig sealed gauge, dynamic pressure sensors (Kulites). All but 32 of the sensors are of type XCEL-10-100-50SG and were mounted perpendicular to the skin surface (Fig. 7b). The remaining 32 were of type LLHT-072 and were mounted in slots horizontal to the surface, in tight places where perpendicular mounting was impossible (Fig. 7a). They were mostly mounted on the lower tower, downstream of the nozzle, and on the subsequent straight and conical sections.

**Data available online at http://windtunnels.arc.nasa.gov/11ft1.html [retrieved December 2012].

Because the horizontal sensors were embedded on the metallic skin of the plenum chamber (just before the nozzle) through which high-temperature gas was flowing, the failure rate was found to be far higher than the perpendicularly mounted counterparts.

The use of active cooling of all electronics inside the model cavity, placement of amplifiers as close to the kulite sensors as possible, transmission of the amplified signal, use of 24 bit analog-to-digital converters, and other precautions translated into clean, relatively noise-free pressure-fluctuation data. Additionally, time traces from each sensor were examined to identify sudden shifts in gain or other tell-tale signs of malfunction. A list of failed sensors was created for each test run; such sensors were excluded from further processing. Therefore, it is believed that the measurement uncertainty for the most part is very low. The noise floor was estimated to be at least 20 dB or more below the minimum level measured on the model. However, the spectral estimates at the high-frequency end, $St > 0.3$, are expected to have a relatively larger uncertainty due to the recess mounting of the sensors. Nominally, the Kulites were recessed by 0.007 in. from the surface. Such a recess produced a small yet important cavity between the sensor tip and the model surface. The cavity was expected to act as a Helmholtz resonator and to create a spurious haystack peak at high frequency. An examination of the spectral data collected without the helium flow and at very low tunnel speed indeed showed the presence of these peaks. However, the resonance peak was found to be a function of the flow speed over the sensor cavity. Data taken without the helium flow but with an increasing wind-tunnel speed showed a progressive lowering of the amplitude and an increase in the frequency of the resonance. This observation is consistent with similar ones made by Hanley [15]. The peaks were either weak or entirely absent for most conditions when the helium plumes were turned on. However, an exact quantification of this uncertainty could not be performed.

### B. Hot-Helium Delivery System

The delivery system was capable of providing hot helium at 700°F and at 610 psia in the plenum chamber inside the model. Central to the helium system was a large heater. After an exhaustive search and review of different options, a natural-gas-fired, $4.4 \times 10^7$ BTU/h (13 MW · h) STAHL heater was selected for the test. In fact, the scope of the test revolved around the capacity of such a heater. The heater was transported from the NASA Glenn Research Center and was slightly modified to suit the test. Natural gas was burned in an airflow supplied by a blower. The heated air was then circulated over a large heat-exchanger coil through which the helium gas flowed. Helium came to the test facility via jumbo trailers (Fig. 8). Typically, two or three trailers, each supplying about 1100 lbm of helium, were used for each day of testing. The trailer outlets were found to be too small to supply the required mass flow rate; therefore, an accumulator was built to temporarily store helium before passing to the heater. When required, helium flowed from the accumulator to the heater. The heat-exchanger coils of the STAHL were preheated to a fixed set point. The large mass of steel in the heat-exchanger pipes acted as thermal capacitors, storing enough energy to quickly bring the helium to the desired temperature. The heated helium flowed through a long pipeline that penetrated the wind-tunnel pressure shell and reached the floor of the test section. A large part of this pipe, upstream of tunnel penetration, was heated using an electrical impedance heater to maintain the gas temperature. Two smaller-diameter pipes delivered helium from the floor of the test section to the sting holding the model. As noted earlier, the hot helium flowed through the hollow sting and then a small settling chamber inside the lower-tower of the LAV model, before exhausting through the four nozzles. The entire helium-delivery system including all control devices and human–machine interface were custom-built for this test. A second part of the gas system was an unheated, high-pressure air supply used for cooling. The model needed to be cooled for any repair and inspection work as well as to change its attitude. The high-pressure air was also used to continuously cool the model cavity that held various instrumentations.

### C. Test Operation

The test was divided into two parts: an integrated system test to thoroughly test the elaborate control system and the final completion of the test matrix. Dynamic pressure data were collected over both phases to maximize the usefulness of helium. The first part of the test provided mostly long data records with progressively increasing plume total temperature and pressure, which may be used to verify scaling laws and other purposes. Data from the second part of the test are presented here. Typically, a test would start when the STAHL reached a preset temperature. At that point, the wind tunnel was brought to the desired Mach and Reynolds number condition, and a volley of hot helium lasting for about 30 s was passed to the model via the heater. Various pipes and valves absorbed a large amount of heat from this first volley, causing the gas temperature in the model


**Fig. 8 A photographic tour of the helium delivery system: a) jumbo trailers and the accumulator; b) STAHL heater; and c) pipes carrying cold and hot helium.**

plenum to not reach its desired set point. The first volley was followed by a second within 1 min. The dynamic data acquisition was started when the plenum pressure and temperature reached target values within an acceptable tolerance. All dynamic pressure sensors were simultaneously sampled at 102, 400/s for 5 s durations. The helium supply was stopped at the end of the data acquisition. The wind-tunnel conditions were changed to the subsequent test point, typically within a few minutes, and the next volley of helium was passed. This operation was continued until the helium pressure in the trailer and the accumulator fell below the usable limit. A typical day used 1500 to 2500 lbm of helium and produced 10 to 15 test points. Note that every helium test point was preceded by a no-flow point when the wind tunnel was operated at the desired $M$ and $Re$ condition yet no helium was passed to the nozzle.

## III. Results and Discussions

Only a glimpse of the large amount of data and images collected from this test could be presented in this paper. Figure 9 shows a simulated abort at the lowest tunnel Mach of 0.3 where the nozzle-exit conditions of the helium plume were closely matched to that expected in the full-scale vehicle. The quality of the shadowgraph images of the helium plumes was better than expected. Note that the horizontal bars in the shadowgraph images are the suction slots on the tunnel wall. One of the bars lay along the centerline of the model. A comparison of the time-averaged photograph of Fig. 9a with the CFD-generated rocket plume of Fig. 1a shows that the distance of the plumes to the vehicle surface is comparable. As expected, the primary difference is a shorter length of the internal shock-cell structure for the helium case. This discrepancy is due to the difference in the ratio of the specific heats, as discussed earlier, and may not have much bearing to the surface pressure fluctuations. The short-exposure photograph of Fig. 9b provides a more insightful description. The acoustic radiation patterns are visible away from the plume. Of more importance is the indication that blobs of turbulent eddies from the outer edge of the plume shear layer impinges on the rear part of the model even at this low forward speed. The primary shear layer is still away from the surface, yet the outer edge scrubs the vehicle surface.



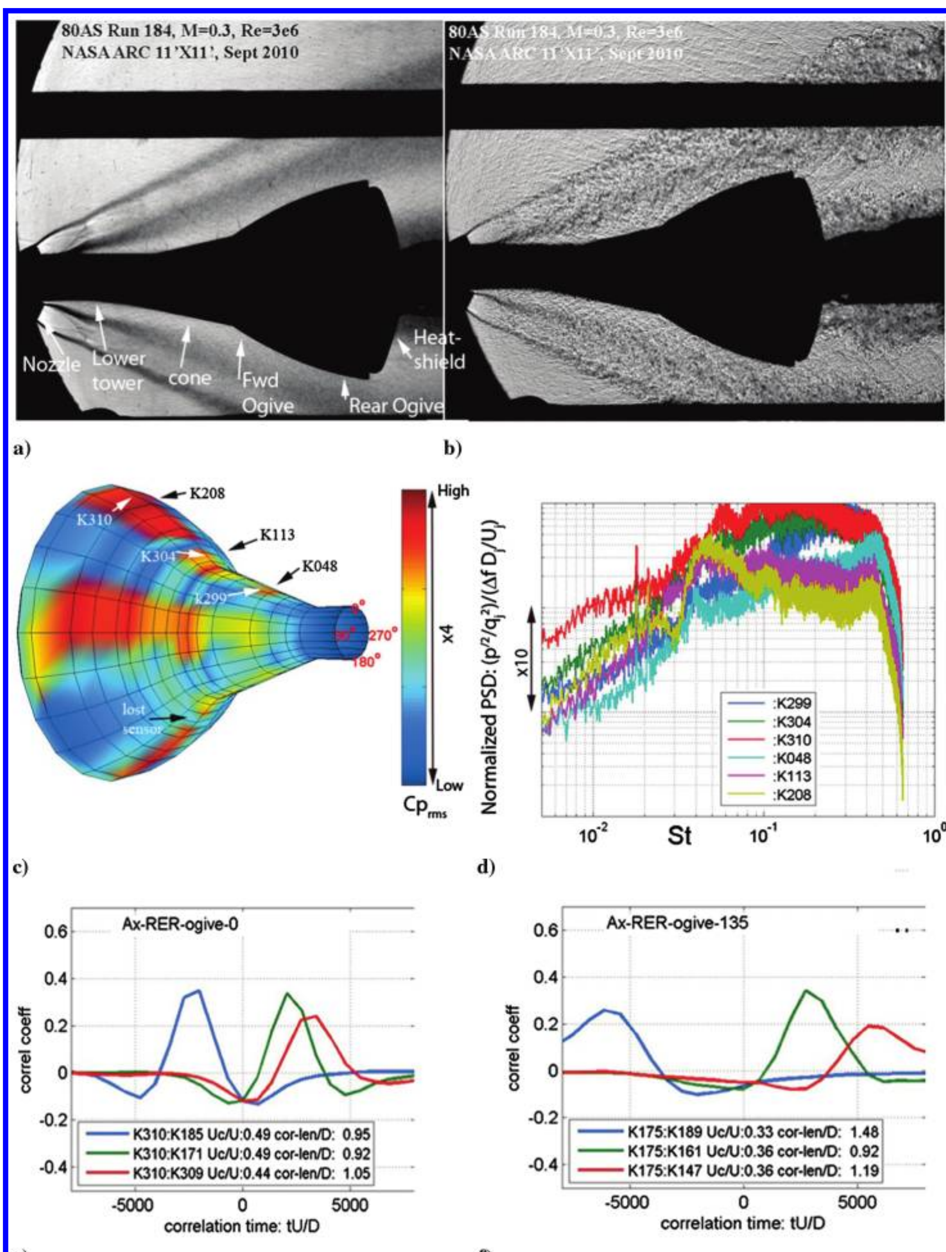


**Fig. 9 Helium simulation of an abort at $M_f = 0.3$ and $\alpha = \beta = 0$ deg. a) Time-average and b) short-exposure shadowgraph images; c) $CP_{rms}$ distribution; d) normalized spectrum of pressure fluctuations; e) correlation among sensors lying underneath a plume axis and, f) similar correlation among sensors in-between two plumes. Tunnel $Re = 3e6/ft$.**

**Table 2 Locations of Kulites shown in psd plots (Fig. 9a shows different zones and Fig. 9c shows locations on LAV)**

| K299 | K304 | K310 | K048 | K113 | K208 |
|---|---|---|---|---|---|
| Under 0 deg plume, cone | Under 0 deg plume, forward ogive | Under 0 deg plume, rear ogive | Between 0 and 270 deg plumes, cone | Between 0 and 270 deg plumes, forward ogive | Between 0 and 270 deg plumes, rear ogive |

Some of the higher-pressure fluctuations in this test were measured in such situations.

Figure 9c shows the distribution of the normalized, overall pressure fluctuations, $Cp_{\mathrm{rms}} = p'_{\mathrm{rms}}/q_{jh}$, on the model surface. The maximum overall level is about 2% of the plume dynamic pressure, which is very high in these high-velocity plumes. The footprints of the four plumes are distinctly visible as regions of higher levels. Note that the interpolation process used in the plotting routine, over the regions where sensor loss occurred, gave the discontinuous appearance in some parts of Fig. 9c.

The normalized psd from two selected groups of sensors are shown in Fig. 9d. The locations of the sensors are shown in Table 2 and in Fig. 9c. For a consistent comparison, spectra measured from the same sensors are shown in all similar figures presented in this paper; also, the same scale/ordinate is used in similar figures. The first group of sensors lay just underneath the 0 deg plume (top plume in the shadowgraph), and the second group is at 45 deg from the first, between two plumes. The narrow-band spectra calculated from the time-traces with frequency resolution $\Delta f$ are normalized using the fully expanded dynamic pressure and Strouhal frequency.

Normalized psd:

$$\frac{p'^2}{q_j^2(\frac{\Delta f D_j}{U_j})} = \frac{(\mathrm{psd})_i}{(q_{jh}^2)(D_{jh}/U_{jh})} \tag{10}$$

Note that the equality of the previous nondimensionalized spectra between the helium plume and the abort-motor plume is the basis for the scaling relationship of Eq. (9). The power spectra from the two groups of sensors are distinct. Sensors from under the plume have peaks around $St \sim 0.2$ and have higher levels; these sensors are relatively unaffected by the freestream. On the other hand, spectra from sensors between two plumes have "flat-top" shape and contain lesser energy.

The normalized correlation coefficients between pairs of sensors, separated in the axial direction, are shown in Figs. 9e and 9f. The convection velocity was measured from the time delay in the correlation peak and from knowledge of the sensor separation. The values were then normalized by the fully expanded plume velocity. The correlation lengths were measured from the magnitudes of the spatial correlation and the separation distance between sensors [16]. The convection velocities were found to be between 30 and 50% of the fully expanded plume velocity. Note that the absolute values are an order of magnitude higher than the ambient sound speed or the speed of the freestream flow. This was found to be true even at higher freestream Mach-number conditions. This observation reinforces the hypothesis that the pressure fluctuations on the vehicle surface are dominated by the very near-field fluctuations of the jet shear layer; the Mach-wave-type acoustic radiation is of secondary importance. The correlation lengths are also comparable to those found in typical plume shear layers [16].

### A. Effect of Increasing Flight Speed

An abort initiated at a higher flight Mach number also means that the abort is occurring at a higher altitude. In the unitary plan, wind-tunnel altitude is simulated by lowering the ambient static pressure with an increase of the freestream speed. Additionally, to bracket all possible altitude conditions for a given flight Mach number, the tunnel Reynolds number was also varied. A lowering of the tunnel Reynolds number translates into a lower ambient pressure and vice versa. Plots of overall fluctuation levels and spectra at Mach 1.2 are shown in Fig. 10. For a better comparison, they need to be contrasted against Fig. 9 ($M = 0.3$). As expected, the shadowgraph images show an increase in the plume diameters with an increase in the flight speed. This increase in the plume diameter also meant an increase in the plume impingement regions on the vehicle surface. Because of its proximity to the nozzle exit, the lower-tower region, just downstream of the nozzle exit, was always a plume-impingement zone and, interestingly, showed the lowest level of fluctuations. The fluctuation levels, however, increased significantly over the cone and the ogive regions, where the shear layers of the plumes were lifted off the body surface. The plume impingement at the rear part of the ogive once again was accompanied by a lowering of the levels. At the transonic $M = 1.2$ condition, shock waves set up on the vehicle (Fig. 10c); however, the accompanying increase in fluctuation levels was relatively small. Examination of the spectra shows a particularly important feature: progressive increase in the low-frequency content from regions under the plume. The structural elements of the vehicle are expected to be more responsive to the low-frequency excitations.

Increasing impingement, causing a decrease in the overall levels of pressure fluctuations, is a significant observation. Impingement is a relative term. Even when the plume is farther away at the $M = 0.3$ condition, an examination of the shadowgraph photos indicate impingement by puffs of turbulent eddies from the outer edge of the plume shear layer on the model surface. As the plume diameter grows in size, the inner part of the shear layer and ultimately the quiescent flow from the plume core impinges on the surface. The level of pressure fluctuations is dependent upon the relative distance of the plume shear layer from the body surface. It is believed that the impingement by the low turbulent quiescent core ultimately causes a reduction of the pressure fluctuations.

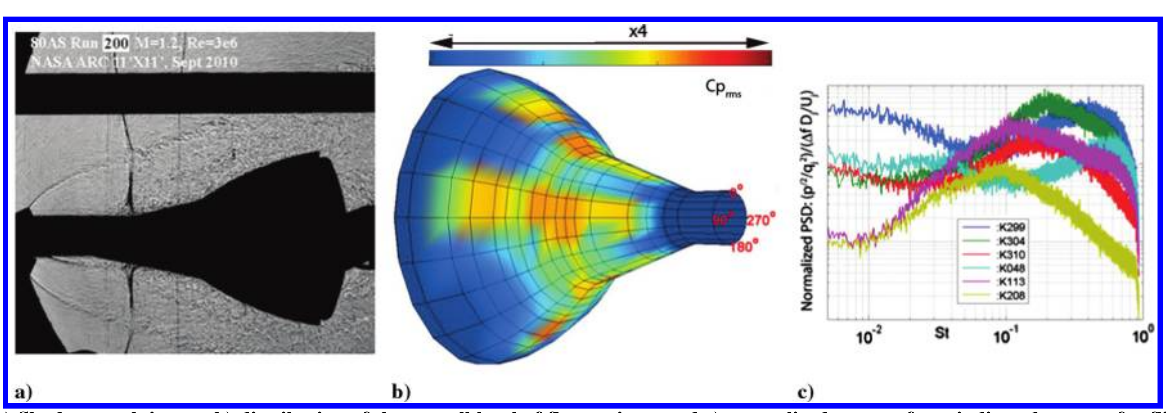


**Fig. 10 a) Shadowgraph image, b) distribution of the overall level of fluctuations, and c) normalized spectra from indicated sensors for flight Mach number $M_t = 1.2$, $Re = 3\mathrm{e}6/\mathrm{ft}$, and $\alpha = \beta = 0$.**

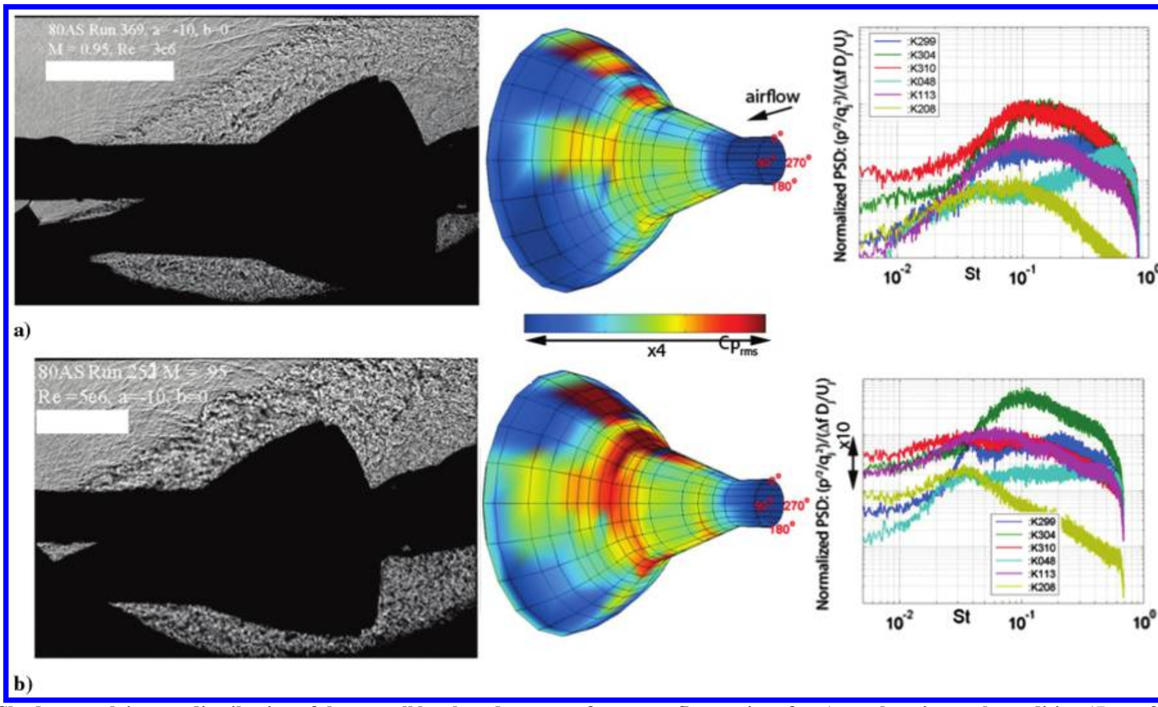


Fig. 11 Shadowgraph image, distribution of the overall level, and spectra of pressure fluctuations for a) nozzle-exit match condition ($Re = 3e6/\mathrm{ft}$), and b) $q$-ratio match condition ($Re = 5e6/\mathrm{ft}$), $M_t = 0.95$, $\alpha = -10$ deg, and $\beta = 0$ deg.

### B. Nozzle-Exit Match Versus $q$-Ratio Match

As mentioned earlier, there were at least two test points taken for each abort condition. The first matched the plume conditions at the nozzle exit, and the second matched the ratio of the dynamic pressures in the freestream and in the fully expanded plume [Eq. (7)]. The latter required lowering the helium supply pressure and increasing in the freestream static pressure. Figure 11 shows a comparison between two such cases for one of the abort simulations. The particular abort simulation was at an angle of attack of $-10$ deg, which destroyed the fourfold symmetry seen in the earlier plots. The

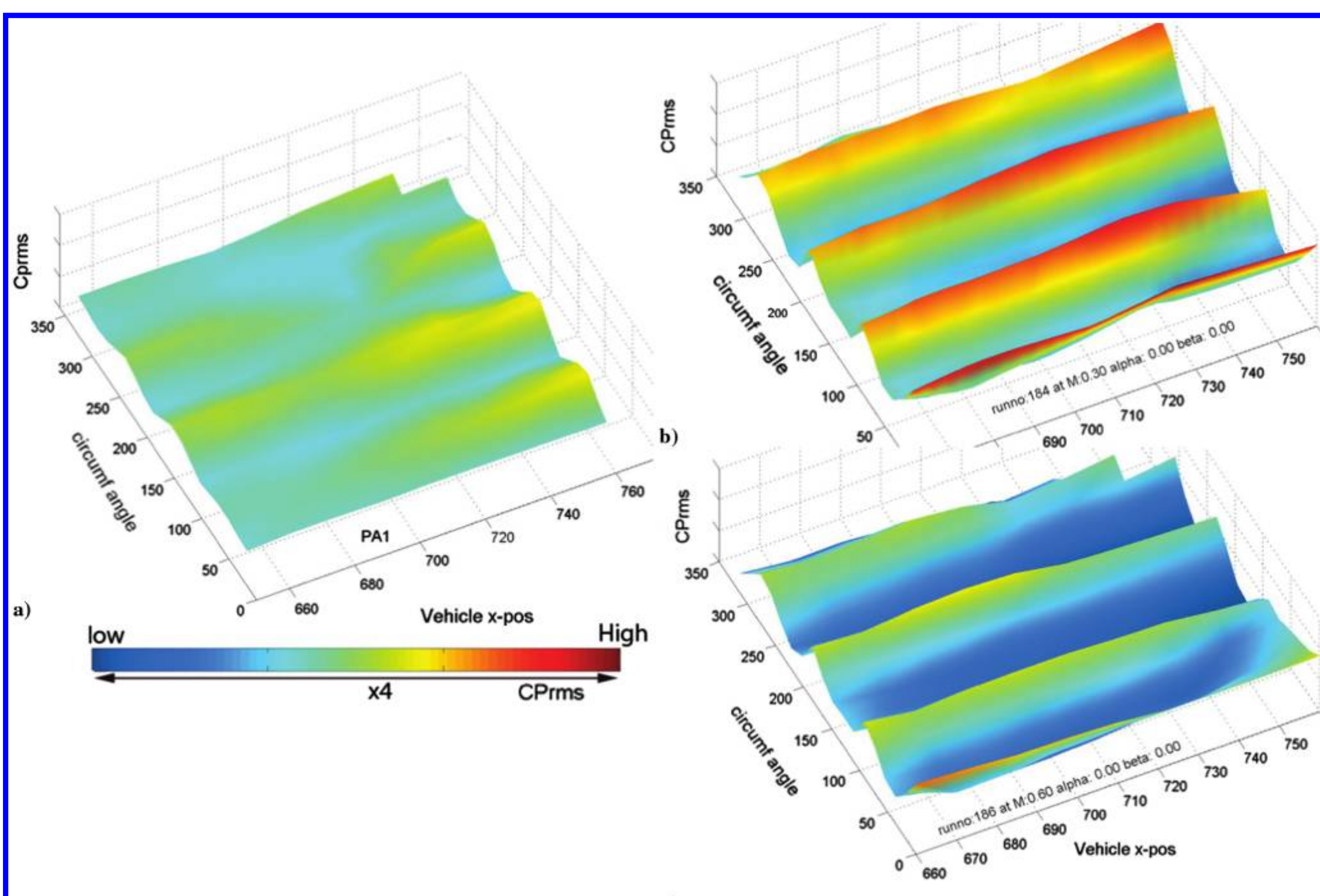


Fig. 12 A comparison of the overall surface pressure fluctuations measured in a) PA1, b) helium simulation at $M_t = 0.3$; c) simulation at $M_t = 0.6$. The same color scale and value ranges were used in all three plots.

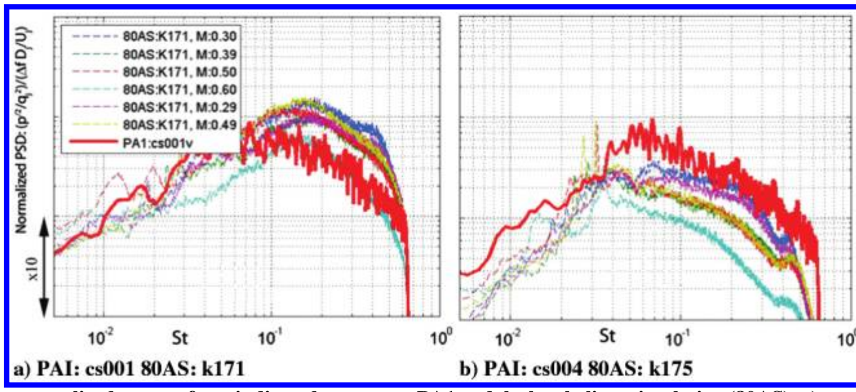


**Fig. 13 Comparison of the normalized spectra from indicated sensors on PA1 and the hot-helium simulation (80AS): a) sensor under the plume axis, and b) sensor between two plumes.**



fluctuation levels on the windward side were found to be higher than the leeward side. Nevertheless, the $q$-ratio match condition was found to produce more-intense fluctuations in spite of a 40% lower thrust from the plume. The plumes from the $q$-ratio matched condition did not grow as large as that from the nozzle-exit match, which also implied that the inner edge of the plume remained unattached to the vehicle surface. It is believed that the reduced impingement has caused an increase in the level of fluctuations.

### C. Comparison with Flight Data from Pad Abort 1

As the AM was lit, the PA1 vehicle quickly gained speed and altitude. Therefore, the flight data were transient and included the influence of a broad range of forward Mach numbers. The Kulite time traces over a flight Mach number range of 0 to 0.65 were used to calculate the overall levels and spectra of surface pressure fluctuations. The wind-tunnel data, on the other hand, were stationary and were collected at fixed Mach number intervals. In Fig. 12, the overall levels measured from the PA1 flight were compared against two helium test points: $M_t = 0.3$ and 0.6. Each plot showed the distributions of $Cp_{\mathrm{rms}}$ on unwrapped vehicle surfaces. The encouraging part was that the helium data nicely bracketed the flight measurements. One interesting difference was the relatively smaller variation between locations underneath the plume and between plumes in the PA1 data. This was attributed to two additional features of the flight data absent from the helium simulation. First, the PA1 vehicle maintained a small nonzero $\alpha$ and $\beta$. As seen earlier, nonzero vehicle attitude makes the plume deviate from a straight path, which can lead to a smearing of the sharp peaks and valleys. Second, in the actual flight, attitude control motors (ACMs) were lit at the top of the vehicle (Fig. 5b) when the AM was burning. The plumes of the ACM solid rockets are expected to add turbulent fluctuations to the incoming stream and can increase the pressure fluctuations in the quieter regions between plumes.

A sensor-by-sensor comparison of the fluctuation spectra is shown in Fig. 13. Note that both flight and wind-tunnel tests used silica-based pressure sensors (Kulite sensors), which have similar frequency response. Because the flight data are an average over a range of Mach numbers, multiple spectra collected from the wind-tunnel simulations over the same Mach range for both the nozzle-exit match and $q$-ratio match conditions are coplotted. Although the spectral shapes are similar in general, the differences seen in the overall levels are also manifested in the individual spectra. For example, sensors directly under the helium-plume axis have spectra that are more energetic, especially in the high-frequency end ($St > 0.1$); the spectra of those in between the helium plumes have less energy compared to their PA1 counterpart. The plausible reasons for such differences are the nonzero attitude angles and the presence of the ACM in the flight test vehicle discussed earlier.

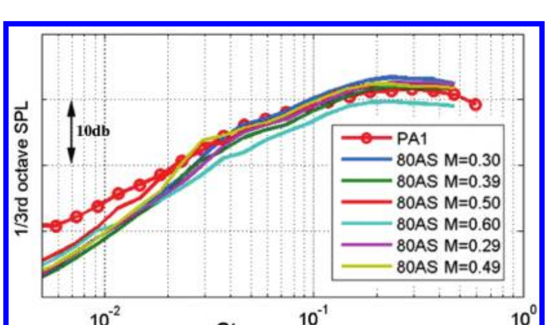


**Fig. 14 Comparison of average spectra from all sensors on PA1 and the corresponding sensors in the hot-helium simulation at indicated Mach numbers.**

Perhaps the best means to overcome difficulties from a varying attitude of the PA1 vehicle is to look into an average spectrum from sensors both underneath and in between the plumes. Figure 14 shows such a comparison. The PA1 spectrum (symbols) was calculated via averaging all sensors downstream of the nozzle exit. Each spectrum from the helium simulation also represents an average over all sensors from comparable locations on the wind-tunnel model. Note that, for this comparison, the helium simulation data were scaled to the flight vehicle condition. Figure 14 shows remarkable similarity between helium spectrum and that calculated from the flight data. The primary difference is in the low-frequency end, where the flight data are more energetic. It is believed that the absence of the afterburning of fuel in the simulated helium plume is the cause of this discrepancy.

## IV. Conclusions

Helium gas heated to 700°F was used to simulate the pressure fluctuations created by the firing of the abort motor (AM) on the surface of the launch-abort vehicle (LAV) over a wide range of flight Mach numbers (0.3 to 1.2) and vehicle attitudes (±14 deg). Compared to other gases, helium provided the best match of the acoustically relevant parameters such as the sound speed, density, and velocity to the solid-rocket plumes. Helium also provided the practicality of test operations, and a cost-effective means of creating 80 different abort scenarios in a wind-tunnel facility. The test was conducted in the NASA Ames Unitary Plan 11-Foot Transonic Wind Tunnel. A custom hot-helium delivery and control system was designed and built for this purpose. A 6% scaled model of the Launch abort vehicle that can withstand the cyclical temperature fluctuations was built and instrumented with 237 dynamic pressure trasducers.

Computational-fluid-dynamics simulations and shadowgraph images taken from the test indicated that the surface pressure fluctuations on the vehicle are primarily dominated by the hydrodynamic fluctuations present in the shear layer of the plumes. Such fluctuations are expected to be scaled by the fully expanded dynamic pressure. The present application involving high forward velocity brought about a large parameter space for matching the wind-tunnel simulation with the actual flight conditions. In a nominal flight, where plume effects are absent, the ratio of dynamic pressures in the wind-tunnel stream, and the flight stream are used to scale model-scale data. The presence of the abort plumes introduced a second ratio: the dynamic pressure in the helium plume to that in the AM plume. To reasonably satisfy a multitude of different matching parameters, two different helium simulations were used to replicate one abort scenario. The nozzle-exit match conditions reasonably replicated the nozzle exit condtion of the AM and were used in past small-scale similarity studies. The new $q$-ratio match conditions allowed for using one scaling equation to include the effects of the different dynamic pressures in the plume and the freestream.

Shadowgraph images collected from the test showed the locations of the plumes at different flight Mach numbers, ambient static pressures, and vehicle attitude conditions. The test data confirmed that an increase in the flight Mach number led to an increased impingement of the plume on the vehicle surface due to an increase of the plume diameters. The distance of the plume shear layer from the vehicle surface was found to play an important role on the overall level of pressure fluctuations. The levels were found to be higher when the shear layer remained separated from the vehicle surface. However, a significant lowering of levels were found to accompany higher impingement when the quiescent part of the plume came in contact with the body surface. This indicates that, for the same attitude, a pad abort will experience a higher level of fluctuations than a higher-altitude abort. The spectra of fluctuating pressure had similar shapes seen in the low-speed plume. An effect of an increase in the flight speed was found to be a progressive increase of the low-frequency part of the spectra.

The scaled up wind-tunnel data were compared with those obtained from the Pad Abort 1 flight test. The acoustic fluctuations on the unmanned LAV surface were measured using dynamic pressure sensors. In spite of various differences in the vehicle shapes, the absence of other control motors in the model test, and the transient-flight condition versus steady-state simulation, it was found that the helium data provided very reasonable comparison with the flight data. The primary difference is a less-energetic low-frequency content of the helium spectra. It is conjectured that some of the unavoidable differences between a solid rocket plume and a helium plume, such as the absence of fuel afterburning in helium simulation, are responsible for this differnce. Neverthless, data obtained from this unique, one-of-a-kind endeavor will provide an aeroacoustics environment for the design and qualification testing of the LAV and many of its subsystems, which are meant to save astronauts' lives.

## Acknowledgements

We are thankful to a very large number of team members whose combined efforts, problem-solving skills, and dedication have made this test possible.

## References

[1] Ffowcs Williams, J. E., "Surface-Pressure Fluctuations Induced by Boundary-Layer Flow at Finite Mach Number," *Journal of Fluid Mechanics*, Vol. 22, No. 3, 1965, pp. 507–519.

[2] Marble, F. E., "Dynamics of Dusty Gases," *Annual Review of Fluid Mechanics*, Vol. 2, 1970, pp. 397–446. doi:10.1146/annurev.fl.02.010170.002145

[3] Pelanti, M., and Leveque, R. J., "High-Resolution Finite Volume Methods for Dusty Gas Jets and Plumes," *SIAM Journal on Scientific Computing*, Vol. 28, No. 4, 2006, pp. 1335–1360. doi:10.1137/050635018

[4] Kinzie, K. W., and McLaughlin, D. K., "Measurement of Supersonic Helium/Air Mixture Jets," *AIAA Journal*, Vol. 37, No. 11, 1999, pp. 1363–1369. doi:10.2514/2.634

[5] Doty, M. J., and McLaughlin, D. K., "Two-Point Correlations and Acoustic Measurements of High-Speed Jets," *8th AIAA/CEAS Aeroacoustics Conference and Exhibit*, AIAA Paper 2002-2553, June 2002.

[6] Papamoschou, D., "Acoustic Simulation of Coaxial Hot Air Jets Using Cold Helium–Air Mixture Jets," *Journal of Propulsion and Power*, Vol. 23, No. 2, 2007, pp. 375–381. doi:10.2514/1.21776

[7] Greska, B., Krothapalli, A., Horne, W. C., and Burnside, N., "A Near-Field Study of High Temperature Supersonic Jets," *14th AIAA/CEAS Aeroacoustics Conference*, AIAA Paper 2008-3026, May 2008.

[8] Greska, B., and Krothapalli, A., "Simulation of Launch Abort System Exhaust Plumes with Downstream Surfaces, Part 2: Heated Helium Plume Test," NASA Rept. (submitted for publication), 2009.

[9] Morgan, W., and Young, K., "Studies of Rocket Noise Simulation with Substitute Gas Jets and the Effect of Vehicle Motion on Jet Noise," Boeing TR ASD-TDR-62-787, Chicago, March 1963.

[10] Tam, C. K. W., and Tanna, H. K., "Shock Associated Noise of Supersonic Jet from Convergent–Divergent Nozzle," *Journal of Sound and Vibration*, Vol. 81, No. 3, 1982, pp. 337–358. doi:10.1016/0022-460X(82)90244-9

[11] Coirier, W. J., "80-AS Aero-Acoustics CFD Support Update," Internal Report Presented to the CEV Loads and Dynamics Group, 2009.

[12] Idicula, J., Williams-Hayes, P., Stillwater, R., and Yates, M., "A Flight Dynamics Perspective of the Orion Pad Abort One Flight Test," *AIAA Atmospheric Flight Mechanics Conference*, AIAA Paper 2009-5730, 2009.

[13] "Unitary Plan Wind Tunnel—11 ft Transonic Wind Tunnel—Standard Operating Procedures," NASA Rept. A327A-7691-XM1, April 2006.

[14] Fong, R., "Final Report for Test 80-AS–Hot-Helium Abort-Motor Plume Aeroacoustics Test," Orion Crew Exploration Vehicle, CEV Aerosciences Project, Rept. EG-CAP-12-66, Oct. 2012.

[15] Hanley, R. D., "Effects of Transducer Flushness on Fluctuating Surface Pressure Measurements," *2nd AIAA Aeroacoustics Conference*, AIAA Paper 1975-534, March 1975.

[16] Panda, J., "Two Point Space–Time Correlation of Density Fluctuations Measured in High Velocity Free Jets," *44th AIAA Aerospace Sciences Meeting and Exhibit*, AIAA Paper 2006-0006, Jan. 2006.

T. Jackson
*Associate Editor*